

# Filters reveal emergent structure in computational morphogenesis

Hazhir Aliahmadi, Aidan Sheedy, and Greg van Anders<sup>a)</sup>

*Department of Physics, Engineering Physics and Astronomy, Queen's University, Kingston ON, Canada*

(Dated: 21 March 2025)

Revolutionary advances in both manufacturing and computational morphogenesis raise critical questions about design sensitivity. Sensitivity questions are especially critical in contexts, such as topology optimization, that yield structures with emergent morphology. However, analyzing emergent structures via conventional, perturbative techniques can mask larger-scale vulnerabilities that could manifest in essential components. Risks that fail to appear in perturbative sensitivity analyses will only continue to proliferate as topology optimization-driven manufacturing penetrates more deeply into engineering design and consumer products. Here, we introduce Laplace-transform based computational filters that supplement computational morphogenesis with a set of nonperturbative sensitivity analyses. We demonstrate how this approach identifies important elements of a structure even in the absence of knowledge of the ultimate, optimal structure itself. We leverage techniques from molecular dynamics and implement these methods in open-source codes, demonstrating their application to compliance minimization problems in both 2D and 3D. Our implementation extends straightforwardly to topology optimization for other problems and benefits from the strong scaling properties observed in conventional molecular simulation.

## I. INTRODUCTION

Computational morphogenesis is a cornerstone of engineering practice, most notably as enacted via iterative methods for optimizing morphology such as topology optimization<sup>1,2</sup>. Recently, topology optimization algorithms have been propelled by major computational advances to unprecedented resolution<sup>3-5</sup>. The rise of ultra-high resolution topology optimization algorithms raises important questions about the comparative performance of as-designed optimal solutions and as-realized physical components: if design precision outstrips manufacturing precision, what forms of deviation between design and realization are permissible (or not) from a performance perspective?<sup>6,7</sup> Arguably, precision advances bring pre-existing design/manufacturing contrast questions into sharper relief. Manufacturing processes typically involve trade-offs between fidelity and throughput, meaning that no design is ever realized with absolute precision in practice.

The ubiquitous discrepancy between design and realization begs for improved understanding, but is complicated by the combination of optimization and emergence. Optimization algorithms are effective at generating solutions, but are less appropriate tools for anticipating real-world performance. Attempts to predict the behaviour of realizations sometimes simulate the physical properties of optimized designs. Using optimal designs to forecast the behaviour of non-optimal realizations is problematic, however, because the analysis is predicated on the anticipation of discrepancies in key features between the hypothetical design and physical reality. Discrepancies between designs and realizations limit the validity of extrapolating from optimal designs to non-optimal designs that are realized in practice. The critical role of non-optimal solutions in anticipating the behaviour of realizations demands new approaches that centre the analysis of non-optimal designs.

New approaches to that address design–realization discrepancies are even more critical because of the conundrum raised by structures with emergent morphology: Computational morphogenesis approaches such as topology optimization provide the greatest design value when they yield structures

---

<sup>a)</sup>Electronic mail: gva@queensu.ca

with emergent morphology. Designs with emergent morphology epitomize the value of topology optimization because the algorithm yields solutions even when the problem formulation provides few clues to the ultimate solution. However, the obscure connection between ultimate, emergent morphology and the original design problem impedes intuitively identifying critical components.

To understand how to make systematic design–realization connections, it is crucial to identify which components of the expected solution contribute most to the design’s purpose. Yet, purpose-based component identification cannot solely rely on perturbative analyses. Perturbative approaches to sensitivity<sup>8,9</sup> and trade-off<sup>10</sup> analyses tend to be limited by the searching method and initial conditions. These limitations indicate the need for more comprehensive, non-perturbative approaches. One set of non-perturbative approaches deployed in other domains of engineering is provided by integral transforms that offer a global perspective on the function being analyzed<sup>11</sup>. For example, the frequency domain techniques<sup>12</sup> that pervade control engineering<sup>13</sup> and signal processing<sup>14</sup> paint a comprehensive picture of underlying behavioural drivers. The success of integral transform techniques in these problems raises the question of whether adaptations exist for non-perturbative analyses of emergent morphogenesis.

Here, we show that Pareto-Laplace transforms<sup>15</sup> of the solution space geometry of a typical computational morphogenesis problem, compliance minimization<sup>2</sup>, yield crucial insights into design–realization relationships and the emergence of structure in computational morphogenesis. Analogous to the time-frequency duality present in problems in signal processing<sup>14</sup>, we find that key morphological features are structural analogs of long-lived transients. We make a precise mathematical identification of the Laplace transform of the solution space volume as a partition function in statistical physics<sup>15</sup>. We leverage this identification to implement the transform using molecular dynamics frameworks<sup>16</sup> that are industry-standard practice in chemistry, physics, and materials science.

We use a statistical physics mapping to show that the geometry of the solution space encodes the emergence of morphology in a discrete set of regimes encoded by temperature in the transformed space. We show that this identification both rationalizes aspects of the emergent structures through a series of condensation regimes and provides a mapping of regions of the system by their importance for overall structural performance. An advantage of our filter-based approach to computational morphogenesis is that it makes it possible to identify the critical elements of an ultimate design without the need to know the full, optimized design itself.

For concreteness, we show results for compliance minimization that we use to compare directly with widely-known, open-source implementations of topology optimization in 2D<sup>17</sup> and 3D<sup>5</sup>. We provide open-source implementations of our methods in MATLAB<sup>18</sup> and C++/Python<sup>19</sup>. Although we give specific results of our methods applied to problems in compliance minimization, our method generalizes straightforwardly to other problems in topology optimization where the design objectives rely on, e.g., electromagnetic, optical, chemical, thermodynamic, hydrodynamic, or acoustic phenomena.

## II. RESULTS

### A. Morphology Emerges Via Distinct Regimes of Structural Condensation

Fig. 1 illustrates the Pareto-Laplace transform for a topology optimization problem, such as compliance minimization for cantilever beam design, using molecular dynamics. We formulate a “molecular” version of the problem by writing a Hamiltonian representing each design domain site as a particle. We assign particles a “position” between 0 (void of material) and 1 (filled with material). The compliance objective generates a gradient force that imparts kinetic energy to particles, which we control using a Nosé-Hoover thermostat. We sample the landscape at a fixed temperature to generate collections of solutions (i.e., a canonical ensemble of solutions<sup>16</sup>), and these solutions elucidate the structure of the solution landscape. (Refer to SI Movie [1] for an animation illustrating a molecular approach to compliance minimization in cantilever beam design at a low temperature.)

From collections of solutions, Fig. 2 shows that low-compliance 2D structures emerge in a process that is analogous to condensation, which occurs via three distinct regimes demarcated by tem-

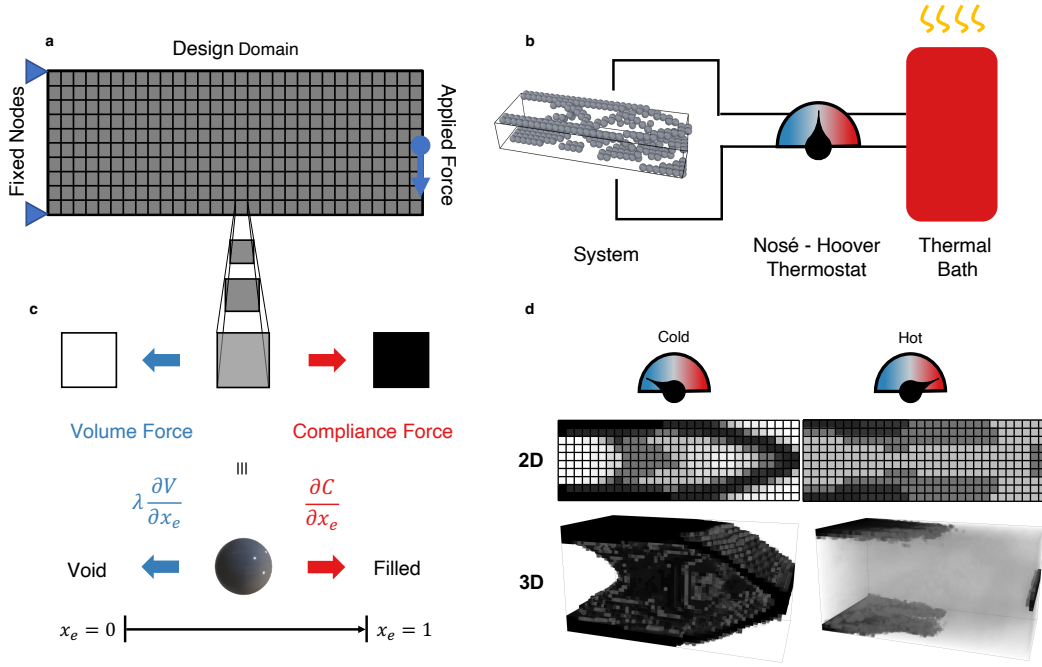


FIG. 1. **The Pareto-Laplace transform for compliance minimization: density dynamics and ensemble generation.** (a) Compliance minimization is about distributing a limited amount of material within a Design Domain to minimize compliance (deformation) under Applied Forces, considering boundary conditions like Fixed Nodes. The density of each site,  $x_e$ , is a value between 0 and 1, where a higher density reduces compliance, while a lower density reduces total used material (volume). (c) The density of each site is analogized to the position of a particle, where forces from compliance and volume constraints influence its position. (b) Connecting the particle system to a heat bath via a Nosé-Hoover thermostat generates an isothermal ensemble of design solutions. (d) shows the average design solutions for low and high-temperature ensembles in 2D and 3D cantilever beam problems.

perature (see Fig. A4 for the 3D cantilever beam). We identified these regimes by computing the compliance ratio, defined as the ratio of the mean compliance of sampled solutions over the solution ensemble to the minimum compliance,  $\langle C \rangle / C_{\min}$ , and the mean pressure  $\langle \lambda \rangle$  required to maintain a total material (volume) fraction  $V_f = 0.5$ . These metrics are presented as functions of temperature in Fig. 2d and Fig. 2e, respectively.

For the regime  $T \gtrsim 20.7$  (all temperatures are given in units of compliance) the first structural features to condense are adjacent sites to the fixed and load-bearing nodes in the cantilever beam problem (see Fig. 2c). We find that this regime coincides with solutions that exhibit  $\langle C \rangle / C_{\min} \gtrsim 3$ , i.e., three times the minimum possible value for the compliance.

For  $T \approx 20.7$  we observe a change in the slope of both  $\langle C \rangle / C_{\min}$  and  $\lambda$  that signals the onset of constraint activation. Between  $17.2 \lesssim T \lesssim 20.7$  the material deposited near the fixed sites remains constant. We note that this behaviour coincides with a steep increase in the mean volume pressure  $\langle \lambda \rangle$  (Fig. 2e) and a near-zero slope for  $\langle C \rangle / C_{\min}$  (which remains at  $\langle C \rangle / C_{\min} \approx 3$ , Fig. 2d). These results indicate that negligible morphological change occurs because the system is increasingly driven to reduce compliance by adding material rather than by condensing existing material.

We find that solutions with  $2 \lesssim \langle C \rangle / C_{\min} \lesssim 3$  emerge for  $3.3 \lesssim T \lesssim 17.2$ , and this reduction in compliance coincides with the condensation of a “frame” connecting the fixed- and load-bearing sites. For  $T \lesssim 3.3$ , we find a near halving of the compliance as it converges to  $\langle C \rangle / C_{\min} = 1$ , which coincides with the condensation of “infill” inside the frame.

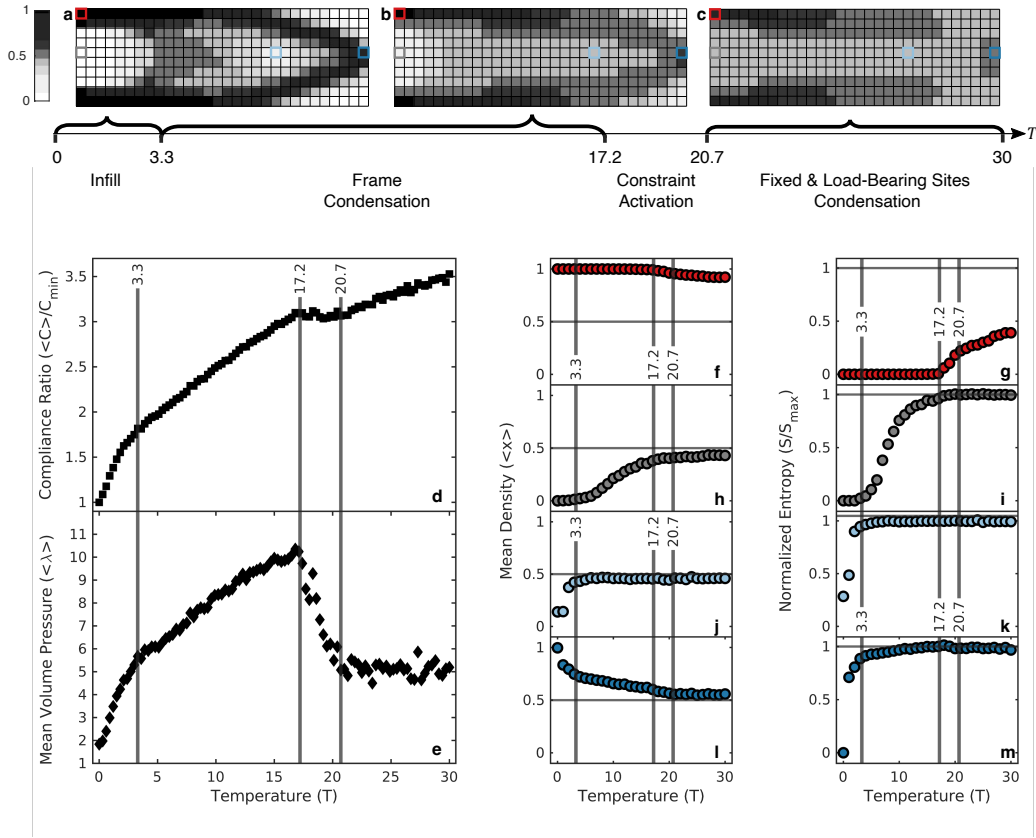


**FIG. 2. Three Phases of Condensation for a 2D Cantilever Beam Problem.** (a–c) mean material distribution at representative temperature regimes: (a)  $T \lesssim 3.3$ , showing infill condensation within the frame; (b)  $3.3 \lesssim T \lesssim 17.2$ , illustrating the formation of a connecting frame; (c)  $T > 20.7$ , highlighting initial condensation near fixed and load-bearing nodes. (d–e) Compliance ratio  $\langle C \rangle / C_{\min}$  and mean pressure  $\langle \lambda \rangle$  as functions of temperature, respectively. For  $17.2 \lesssim T \lesssim 20.7$ , the mean volume pressure increases sharply, while the compliance ratio remains nearly constant, indicating that the reduction in compliance is due to the addition of material rather than condensation. (f–m) Site-specific Mean density  $\langle x \rangle$  and entropy density  $S/S_{\max}$  across four representative sites: (f, g) An essential site to compliance minimization (red square in (a–c)), exhibiting high density and low entropy even at high  $T$ . (h, i) A site with a contribution to volume reduction rather than compliance minimization (gray square in (a–c)), characterized by simultaneous loss of density and entropy at  $T \approx 20$ . (j, k) A designable site (light blue square in (a–c)) maintains high entropy and  $\langle x \rangle$  until  $T \approx 3.3$ . (l, m) A sensitive site (dark blue square in (a–c)) converges to its final density at higher  $T \approx 20$  while preserving entropy down to  $T \approx 3.3$ .

## B. Optimal Solutions Depend on All Sites but with Different Roles

The emergence of morphology via a series of distinct regimes of structural condensation can be ascribed to a corresponding set of microscopic, site-specific behaviours. Fig. 2 panels f,h,j,l show mean material density (referred to as mean density hereafter),  $\langle x \rangle$ , as a function of temperature for four representative sites (corresponding data for all sites are given in Fig. A1) and Fig. 2 panels g,i,k,m show entropy density,  $S/S_{\max}$ , as a function of temperature for the same four representative sites (corresponding data for all sites are given in Fig. A2). This analysis reveals a range of sensitivity among sites in minimizing compliance, where some sites rely on the contributions of other sites and the overall design, while others act independently and are essential for achieving compliance reduction. (Refer to Appendix C for details on entropy calculation.)

Fig. 2f,g show the mean density and entropy density of a representative site that is essential to minimizing compliance. This site (identified by a red square in Fig. 2a,b,c) has high mean density,



$\langle x \rangle \approx 1$ , and low entropy density,  $S/S_{\max} < 0.5$ , even at high temperatures,  $T \gtrsim 20$ . However, low entropy density at high temperatures is insufficient to conclude a site’s role in the overall design. Fig. 2h,i correspond to a representative site (indicated by a grey box in Fig. 2a,b,c) that makes a negligible contribution to overall compliance minimization. This is signaled by a coincident loss in entropy density and in mean density beginning at relatively high temperature  $T \approx 20$ . In effect, these sites contribute to the design by reducing volume rather than compliance.

In contrast to the sites marked with red and gray squares in Fig. 2a,b,c, some sites reach maximum entropy at much lower temperatures. The behaviour of these sites can be classified by considering their mean density. The sites, like the one marked with a light blue square in Fig. 2a,b,c, are designable, which maintain high entropy density  $S/S_{\max} \approx 1$ , and mean density  $\langle x \rangle \approx 0.5$  down to relatively low temperatures,  $T \approx 3.3$  as shown in Fig. 2j,k. The other ones, like the site indicated by a dark blue square in Fig. 2 a,b,c, are sensitive and start to converge to their final density at high temperature ( $T \approx 20$  in this case), yet preserve high entropy down to low temperature ( $T \approx 3.3$  in this case).

### C. Condensation Temperature Map Signals Site-Specific Importance

Site-specific results reported in Fig. 2 indicate that although all sites contribute to minimizing compliance at a fixed volume, different sites play very different roles. We associated roles with quantifiable behaviours, and we can further assign relative importance to individual sites.

Fig. 2 provided a set of indicators that signal distinct roles for different sites. However, reporting these indicators for all sites would be cumbersome, particularly for extensions to compliance minimization in three dimensions, so it is instructive to use a proxy. To define this proxy, we note Fig. 2 indicates a clear association between overall compliance and temperature, so we classify importance using condensation temperature for each site. We defined the condensation temperature for a site as the temperature at which  $S/S_{\max} < 0.85$ , where the site’s density behaves like a gas.

Fig. 3 shows importance maps for compliance minimization of a cantilever beam in two- and three dimensions. For the 2D problem, Fig. 3a shows an optimized solution adjacent to the condensation temperature map, see Fig. 3b. Fig. 3d depicts the importance map that results from composing the optimal solution and the condensation temperature map using the colour density map depicted in Fig. 3c. The most important sites, indicated in red, are sites that condense at very high temperatures, i.e., those sites are essential to be filled even for designs with a moderate level of compliance. Less important sites, shown in blue, condense only at low temperatures. These sites are considered designable; although they are included in the optimized solution, manufacturing errors affecting their density do not compromise the optimality of the design as much as for red or gray sites.

Fig. 3e gives a corresponding importance map for a 3D cantilever beam. Like the 2D case, results indicate that the sites adjacent to the fixed sites are among the most important. However, in the 3D case, this importance is shared by the load-bearing sites. (Refer to SI Movie [2] for an animation showcasing the 3D map from all angles, and see Fig. A5 for further details on the importance map related to the 3D cantilever beam problem.)

### D. Effective Dimensionality Facilitates Overall Design Characterization

We observed that structures condense non-uniformly as a function of temperature to reduce compliance in a series of regimes. Each regime that results in a compliance reduction is associated with a set of sites. We mapped how compliance reduction depends on different sites via the importance maps shown in Fig. 3. However, it is easy to imagine cases where it is important to extract broader-level design information in addition to the granular understanding of a single design. The behaviour of the compliance–temperature response signals the underlying geometry of the solution space which is a key indicator for this class of comparisons.

Fig. 4 gives an annotated plot of  $\langle C \rangle$  vs  $T$  for a 2D cantilever beam. As we noted above, the condensation regimes are indicated by a series of approximately linear responses. In conventional physical systems,  $\langle C \rangle (T)$  would be referred to as an equation of state, and its form would reflect

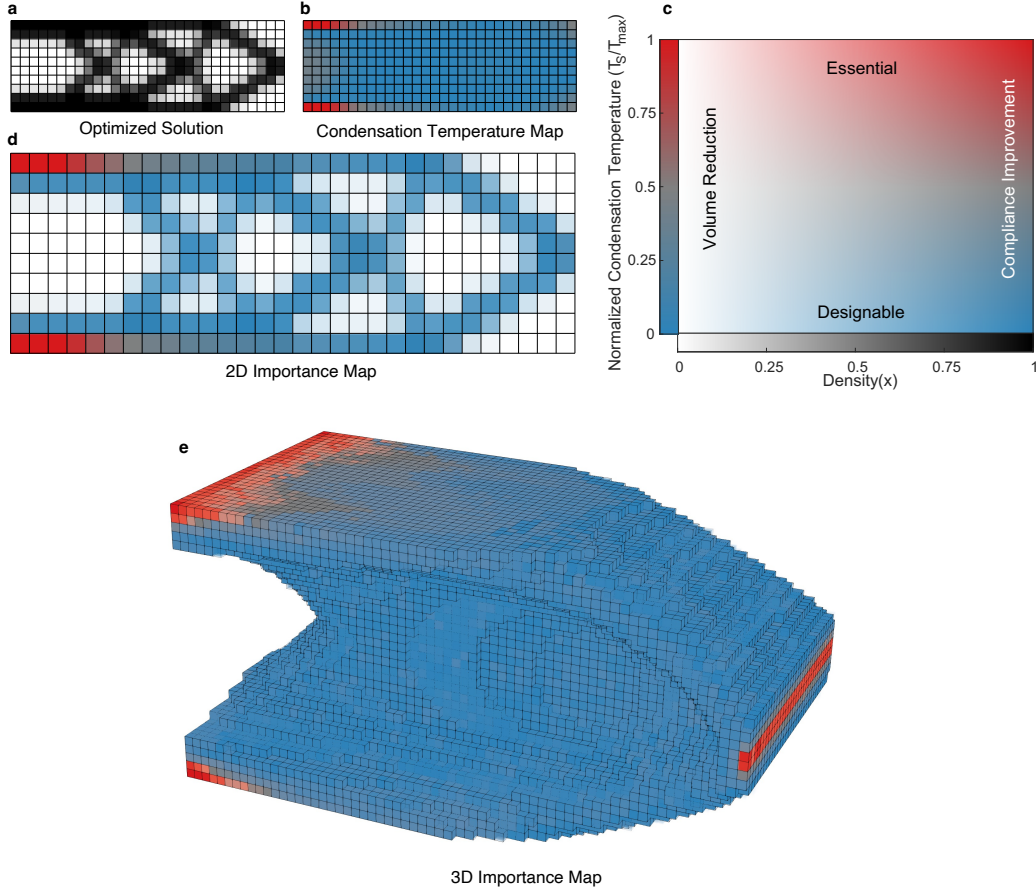


FIG. 3. **Importance Maps for 2D and 3D Cantilever Beam Design Problems.**(a) An optimized solution as solved by<sup>17</sup>. (b) The Condensation Temperature Map, showing the normalized condensation temperature across the design domain with the colormap in (c), assuming a filled density ( $x_e = 1$ ) for all sites. (c) shows a 2D colormap where the horizontal axis represents site density and the vertical axis shows the normalized condensation temperature. The vertical axis indicates site importance, with higher condensation temperatures marking essential sites and lower temperatures indicating designable ones. High-density sites (opaque) contribute to compliance minimization, while low-density sites (transparent) aid in volume reduction.(d) The Importance Map for the 2D Cantilever Beam, based on the optimized solution in (a) and the Condensation Temperature Map in (b), using the colormap provided in (c). (e) The Importance Map for the 3D Cantilever Beam.

the structure of the underlying state space. Here, the state space is the solution space, and so the behaviour of the solution space must signal how optimized designs emerge.

In Methods (see, Sec. IV E) we use the Pareto-Laplace transform to derive a theory that relates the slope of the compliance–temperature to the growth of the number of candidate designs with fixed, non-minimal compliance. We consider a regime where the number of candidate designs, denoted as  $\Omega$ , follows the scaling relation

$$\Omega(C) \sim (C - C_{min})^{\frac{N_{IP}}{\nu} - 1}, \quad (1)$$

where  $\Omega(C)$  increases with  $N_{IP}$ , the effective number of “in-play” dimensions. Here,  $N_{IP}$  represents the number of sites capable of participating in a correlated exchange of material while maintaining the fixed level of mean compliance under a constant total volume constraint. The parameter  $\nu$  serves as a growth index; for instance, if the volume of solution space scales linearly with the number of sites,  $\nu = 1$ . In Section IV F, we demonstrate that this growth leads to the following

expression for the compliance–temperature slope:

$$\frac{\partial \langle C \rangle}{\partial T} = \frac{N_{IP}}{\nu}, \quad (2)$$

where this slope encodes the effective number of “in-play” sites at a given compliance level.

We derive Eq. (2) in Sec. IV E, and IV F, but to see how this arises on more than purely mathematical grounds, it is useful to form an approximate grouping of sites into one of three, temperature-dependent states: unconstrained, in-play, or condensed. At a given temperature, condensed sites, akin to particles in a solid, have essentially fixed material density and vanishing entropy density. Unconstrained sites, akin to particles in a gas, have  $\langle x \rangle \approx 0.5$  and maximal entropy density, and fluid-like in-play sites are in the process of condensing and constitute degrees of freedom that affects the solution space at that temperature.

Condensed sites do not contribute to  $\Omega(C)$ , and therefore do not contribute to  $\langle C \rangle(T)$ , because their degrees of freedom are effectively “frozen out”. Unconstrained sites also contribute to neither  $\Omega(C)$  nor  $\langle C \rangle(T)$ , however rather than being frozen out, those gas-like sites are unaffected by the objective function or constraints at a given  $T$ . The only sites that do contribute are the fluid-like, in-play sites, that engage in a correlated exchange of material to maintain some fixed level of mean compliance for a constant total volume.

The slope of  $\langle C \rangle$  vs  $T$  in 4a provides a direct estimate of the relative size of regions involved in the formation of structure at a fixed level of compliance. For the 2D cantilever beam, we are able to confirm this site classification directly by mapping individual sites in Fig. 3b,c,d (Refer to SI Movie [3] for an animation illustrating how the sites condense as the temperature decreases.). However, this approach could also be repeated for larger-scale systems with large numbers of sites where the granular visualization of individual sites is impractical.

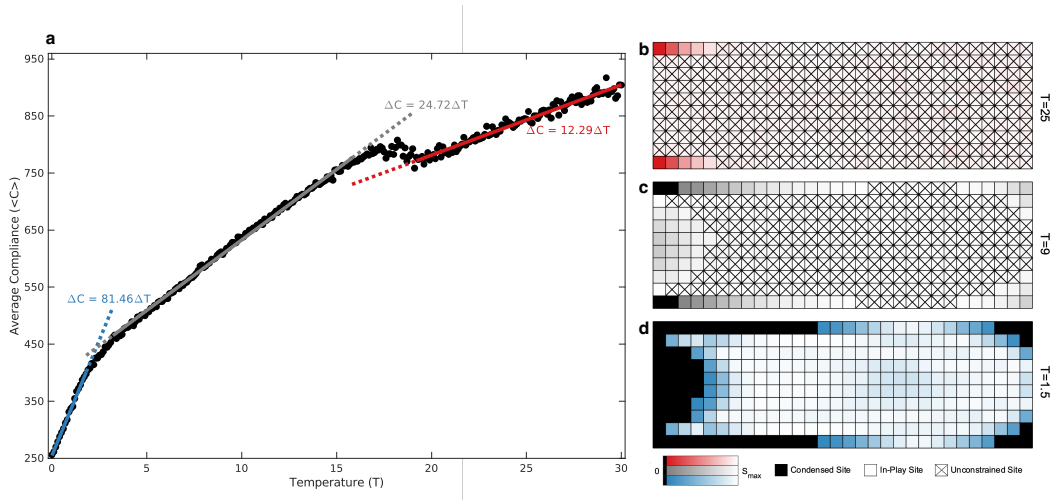


**FIG. 4. Linear Response of Average Compliance to Changing Temperature.** (a) Different slopes of the linear response indicate distinct regimes of condensation, each with a different number of effective dimensions. (b) At  $T = 25$ , most sites are unconstrained with maximized entropy, and only the few in-play sites contribute to reducing compliance, resulting in the linear behavior is shown by the red line in (a). As temperature decreases to  $T = 9$ , more sites become condensed, leading to more in-play sites and a higher slope of the linear response, as illustrated by (c) and the grey line in (a). (d) shows the design domain at  $T = 5$ , where most sites are in-play, optimizing the infill design to minimize compliance.

### III. DISCUSSION

We showed that integral transforms of solution spaces in topology optimization provide new forms of insight into design–realization contrasts in computational morphogenesis. Our approach

supplements powerful, widely-used methods for topology optimization, which emerge as a zero-temperature limit of our approach. Though we give explicit results for problems in compliance minimization at scales that facilitate comparison with well-known results in topology optimization, our methods are straightforward to extend.

Topology optimization has been demonstrated for a wide range of problems, e.g., material design<sup>20–22</sup>, photonic structures,<sup>23,24</sup> microfluidics,<sup>25–27</sup> heat transfer,<sup>4,28</sup> among many others. The key feature that makes topology optimization portable across all of these domains is that in each application, the only difference is the underlying partial differential equation that links solution morphology to the design objective. Our Nosé-Hoover thermostat-based, molecular dynamics implementation of the compliance minimization Laplace transform is, in essence, a “superset” of gradient-based topology optimization. Any gradient-based topology optimization problem could be “lifted” using the same set of mathematical procedures we employ here. Indeed, we are engaged in molecular dynamics-based extensions of the present methodology to topology optimization problems in other domains, which we hope to report on soon.

Although the specific numerical results we report here were computed with a molecular dynamics-based algorithm, the insights they provide stem from the more foundational structure which is the Pareto-Laplace transform<sup>15</sup> of the solution space geometry. Laplace transforms of the sort we derive here have been employed in statistical physics for more than a century, and advanced methods have been derived for computing them in cases where there is no well-defined notion of a gradient. Consequently, we anticipate that the proposed approach will extend to non-gradient topology optimization problems.

We gave examples of filter-based analyses using example codes in MATLAB<sup>18</sup> and a Petsc-based C++ implementation<sup>19</sup>. However, because the approach relies on molecular dynamics techniques, other implementations of filter-based analyses could deploy advanced sampling methods<sup>16</sup> or could take advantage of the strong scaling of molecular dynamics to thousands of graphics processing units<sup>29</sup>. We should also note that although we used a Nosé-Hoover thermostat, other methods of thermostating, e.g., via a Langevin thermostat<sup>30</sup>, might find use in other settings.

Finally, we note that the filter-based approach we present above show it is possible to predict a design’s most important elements without knowing the final design’s full form. This signals that filters could be deployed as a leading indicator in an iterative, complex design process. In addition, although we focused on the emergence of structure through condensation, applying our filter approach to “evaporate” designs could provide important training data for generative AI methods for engineering structures that mimic techniques used for image generation.

## IV. METHODS

### A. Compliance Minimization

Topology optimization problems typically involve the deposition of material in a fixed design domain according to some optimization criterion. For concreteness, we will consider compliance minimization, however, the framework we present below extends straightforwardly to other forms of topology optimization problems.

Compliance minimization, invokes the problem to

$$\begin{aligned} \min_x C &= \int_{\Gamma} dV f(u(x), x) \\ \text{s.t. } \int_{\Gamma} dV x &= V_0, \end{aligned} \tag{3}$$

where  $C$  is the compliance,  $x$  is the material density over the domain,  $\Gamma$ , with volume element  $dV$ , and total material volume  $V_0$ . Compliance is taken as the integral of the strain energy density,  $f(u(x), x)$ , where the displacement,  $u(x)$ , satisfies the stiffness equation<sup>2</sup>. Topology optimization approaches minimize compliance by making a finite-element approximation and invoking gradient-based algorithms<sup>17,31</sup>.

## B. Pareto-Laplace Filter

We express the number of possible design solutions,  $\{x\}$ , with a given compliance and fixed material volume  $V$  as  $\Omega(C, V)$ <sup>32</sup>, and apply the Pareto-Laplace filter

$$Z(\beta) = \int_{C_{\min}(V)}^{\infty} dC e^{-\beta C} \Omega(C, V), \quad (4)$$

where  $\beta$  plays the role of the Laplace variable, and  $C_{\min}$  is the minimum possible value for the compliance at fixed material volume  $V$ .  $\Omega(C, V)$  encodes the “volume” of patterns of material distribution that realize a compliance of  $C$  and have physical material volume  $V$ . The quantity  $Z(\beta)$  aggregates those volumes to give a total “mass” of the solution space for all possible  $C$ , where the weighting factor for a solution, like  $x$ , is given by  $w(C) = e^{-\beta(C(x)-C_{\min})}$ . Mathematically,  $Z(\beta)$  is a generating function that is a weighted sum over the number of ways of realizing designs of fixed compliance and material volume, and so it encodes the geometry of the solution space<sup>15</sup>.

The interpretation of the Laplace transform in Eq. (4) is analogous to the time/frequency domain contrasts that inform other areas of engineering. As  $\beta \rightarrow \infty$ , only solutions  $\{x\}$  for which  $C \approx C_{\min}$  contribute, and hence  $Z(\beta \rightarrow \infty)$  is dominated by near minimum solutions. Hence, in the limit  $\beta \rightarrow \infty$ , one recovers the original compliance minimization problem.

As  $\beta \rightarrow 0$ , all solutions receive equal weight, regardless of their compliance. The rate at which  $Z$  decreases as  $\beta$  goes from 0 to  $\infty$  encodes the growth of  $\Omega(C, V)$  with  $C$ , analogously to the way that frequency space encodes transients in time domain problems.

## C. Filter Implementation

Though Eq. (4) geometrizes the solution space in the form of a Laplace transform, in practice it is not possible to directly evaluate the integral, not only because  $C_{\min}(V)$  is a primary unknown quantity in the original formulation of the problem in Eq. (3), but also because  $\Omega(C, V)$  is not known. However, analogous density of states transforms are ubiquitous in statistical physics, where closed-form evaluation is only possible in a very small minority of cases, see e.g.<sup>33</sup>. In the majority of cases, a variety of analytic and numerical techniques facilitate working directly in terms of the underlying degrees of freedom<sup>34</sup>.

For compliance minimization, the underlying degrees of freedom are given by the design field  $\{x\}$ . It is convenient to work with the discrete approximation<sup>35</sup>, where Eq. (4) can be rewritten as

$$Z(\beta) = \sum_{\{x\}} e^{-\beta C} \delta \left( \sum_e x_e - V \right). \quad (5)$$

where compliance,  $C$ , is evaluated for each solution ( $x$ ), with each solution representing a set of densities,  $\{x_e\}$  and  $\delta$  is a Dirac delta function that enforces the material volume constraint.

Eq. (4), and the equivalent form Eq. (5) geometrize the compliance-minimization solution space. In statistical physics  $\beta = 1/T$ , where  $T$  is thermodynamic temperature. There are well-defined computational techniques, see, e.g. Ref.<sup>16</sup>, that provide statistical sampling that can generate the distributions of  $\{x\}$  that contribute to  $Z(\beta)$  up to arbitrary accuracy.

## D. Physical and Statistical Interpretation

Laplace transforms, Eq. (5), are typically not possible to evaluate in closed form. However, as a mathematical construction, Eq. (5) has the form of a partition function used for more than a century in statistical physics<sup>33</sup>. Notably, along with the thermodynamic interpretation of  $Z(\beta)$ , the connection between thermodynamics and statistical mechanics, see, e.g. Refs.<sup>33,36</sup>, dictates that  $Z(\beta)$  can also be interpreted as a generating function for probability distributions. From a probabilistic point

of view, that facilitates the computation of statistical averages over the solution space, e.g.,

$$\langle C \rangle = \frac{1}{Z(\beta)} \int_{C_{\min}}^{\infty} dC e^{-\beta C} \Omega(C, V) C, \quad (6)$$

where the notation  $\langle \cdot \rangle$  indicates the so-called thermal or ensemble average. Note, that by inspection we must have that

$$\langle C \rangle = -\frac{\partial \ln(Z(\beta))}{\partial \beta}, \quad (7)$$

which provides a clearer indication of how  $Z(\beta)$  generates a probability distribution<sup>15</sup>.

### E. Near Optimal Expansion

Considering the global minimum at some compliance  $C_{\min}$ , then the volume of the solution space will vanish for  $C < C_{\min}$ . In that case, suppose that for values of compliance that fall just above  $C_{\min}$  we can approximate the solution space volume

$$\Omega(C, V) \propto (C - C_{\min})^{\frac{N_{IP}}{\nu} - 1}, \quad (8)$$

where  $N_{IP}$  is the effective number of degrees of freedom in play near the minimum and  $\nu$  is an index of growth. In this case, we can evaluate Eq. (4) directly, which gives us

$$Z(\beta) \propto e^{-\beta C_{\min}} \beta^{\frac{N_{IP}}{\nu}}, \quad (9)$$

where we have dropped negligible overall multiplicative constants. That means that in the limit of large  $\beta$  or, equivalently, low temperature  $T$ , we can estimate Eq. (7) to be

$$\langle C \rangle \approx C_{\min} + \left( \frac{N_{IP}}{\nu} \right) T. \quad (10)$$

### F. Beyond Near-Optimal Design

Consider the case where some degrees of freedom are “in play” near the minimum, up to some saturation point,  $C_*$ , after which a different set of degrees of freedom comes into play. We represent this by

$$\Omega(C, V) = \begin{cases} \gamma_{<} (C - C_{\min})^{\frac{N_{<}}{\nu} - 1} & C < C_* \\ \gamma_{<} (C_* - C_{\min})^{\frac{N_{<}}{\nu} - 1} + \gamma_{>} (C - C_*)^{\frac{N_{>}}{\nu} - 1} & C > C_* \end{cases}, \quad (11)$$

where  $\gamma_{<,>}$  are geometric coefficients, and  $N_{<,>}$  are scaling exponents giving the number of effective degrees of freedom for  $\Omega(C, V)$  on either side of  $C_*$ .

Integrating Eq. (11) gives

$$Z(\beta) = e^{-\beta C_{\min}} \beta^{\frac{N_{<}}{\nu}} \gamma_{<} \left[ \Gamma\left(\frac{N_{<}}{\nu}\right) - \Gamma\left(\frac{N_{<}}{\nu}, \beta(C_* - C_{\min})\right) \right] + e^{-\beta C_*} \beta^{\frac{N_{>}}{\nu}} \left[ \gamma_{>} \Gamma\left(\frac{N_{>}}{\nu}\right) + \gamma_{<} (\beta(C_* - C_{\min}))^{\frac{N_{>}}{\nu}} \right]. \quad (12)$$

where  $\Gamma(\cdot, \cdot)$  is the incomplete Gamma function.

We can use this to find that for  $\beta(C_* - C_{\min}) \gg 1$  (equivalently  $T \ll C_* - C_{\min}$ ),

$$\langle C \rangle \approx C_{\min} + \frac{N_{<}}{\nu \beta} = C_{\min} + \left( \frac{N_{<}}{\nu} \right) T, \quad (13)$$

whereas for  $\beta(C_* - C_{\min}) \ll 1$  (equivalently  $T \gg C_* - C_{\min}$ ),

$$\langle C \rangle \approx C_* + \frac{N_{>}}{\nu\beta} = C_* + \left( \frac{N_{>}}{\nu} \right) T. \quad (14)$$

Note that for  $T \ll C_* - C_{\min}$  and  $T \gg C_* - C_{\min}$ ,  $C$  asymptotes to linear response in  $T$ . In both cases, the slope is determined by the power law growth of  $\Omega(C, V)$ . The exponent in this power law growth is, in turn, determined by the number of degrees of freedom that are “in play” at that level of  $T$  (or  $\beta$ ).

## G. Numerical Integral Transform Implementation

Casting the Pareto-Laplace transform of Compliance minimization in the equivalent form of Eq. (5) unlocks a vast array of techniques in physics, chemistry, and materials science that developed to handle analogous problems.

To generate the material distributions  $\{x_e\}$  that contribute to Eq. (5), we identify  $Z(\beta)$  as a partition function with compliance as the potential energy  $U = C(\{x\})$ , and fixed temperature  $T = \frac{1}{\beta}$ . We treat material densities as “particles”, where each particle is fixed to a position  $x_e$  in the design domain, and its “position” in an auxiliary dimension describes the density of material in that cell (no material :  $x_e = 0$ , filled cell:  $x_e = 1$ ). It will be convenient to visualize the “filling” dimension as perpendicular to the design domain.

With this framing, the task of computing  $\Omega(C, V)$  is equivalent to generating a volume-preserving series of solutions. However, since we are interested instead in computing  $Z(\beta)$ , we must generate a series of configurations appropriate to that quantity. For systems of conventional particles, this task represents the central challenge in molecular simulation, and it is one of the first problems that was tackled with scientific computing, so a vast literature has emerged over the last several decades<sup>16,37</sup>. As such, a variety of means exist for computing Eq. (5), and so the approach that we develop here is a powerful but first means of obtaining traction.

Our approach implements the computation of Eq. (5) by exploiting an analogy with industry-standard implementations of the framework of molecular dynamics used in chemistry, physics, and materials science. The approach we take here for topology optimization most closely mirrors the treatment that Ref.<sup>37</sup> develops for conventional systems. For more details on the numerical implementation of the integral transform using molecular dynamics for topology optimization, refer to Appendix A.

## ACKNOWLEDGMENTS

We thank I. Babayan for useful discussions and comments on the manuscript, and R. Perez for discussions that initiated this investigation and collaboration at an early stage of the project. We acknowledge the support of the Natural Sciences and Engineering Research Council of Canada (NSERC) grants RGPIN-2019-05655 and DGEER-2019-00469. Computations were performed on resources and with support provided by the Centre for Advanced Computing (CAC) at Queen’s University in Kingston, Ontario. The CAC is funded by: the Canada Foundation for Innovation, the Government of Ontario, and Queen’s University.

## Appendix A: More Details on Numerical Integral Transform Implementation

A full description of molecular dynamics is beyond the scope of this manuscript, but the key to computing Eq. (5) is the introduction of two sets of auxiliary variables. For defining the first set of auxiliary variables, if we regard the density of material at each point as the “position” of a particle that determines potential energy (vis-a-vis compliance), then it is possible to introduce a kinetic

energy for the particles that associates a momentum with each position. One can then multiply Eq. (5) by one in the form of

$$1 = \frac{\prod_{x_e} \int_{-\infty}^{\infty} dp_e e^{-\beta p_e^2}}{Z_{\text{free}}(\beta)}, \quad (\text{A1})$$

where the factor in the numerator corresponds with the definition of  $Z_{\text{free}}$  in the denominator. It is straightforward to show that  $Z_{\text{free}} = (\frac{\pi}{\beta})^{N/2}$ , where  $N$  is the number of elements to deposit material in. With this factor, Eq. (5) is equivalent to

$$Z(\beta) = \left(\frac{\beta}{\pi}\right)^{\frac{N}{2}} \sum_{\{x,p\}} e^{-\beta(\sum_e p_e^2 + C)} \delta\left(\sum_e x_e - V\right), \quad (\text{A2})$$

where the sum should be interpreted schematically. Note that by adding degrees of freedom that have the form of momentum, Eq. (A2) is mathematically equivalent to our original quantity of interest, however, by explicitly introducing momentum we are able to induce dynamics to generate configurations of the design field.

Ensuring that the induced dynamics generates configurations of the design field that correctly reproduce the integral in Eq. (4) requires introducing a second set of auxiliary variables. The integrand in Eq. (A2) depends on the quantity

$$\mathcal{H} \equiv \sum_e p_e^2 + C \quad (\text{A3})$$

which has the form of a Hamiltonian in classical mechanics, e.g. c.f. Ref.<sup>38</sup>. Hamiltonians of this form generate dynamics that conserve energy, however the form of Eq. (5) indicates that we require instead dynamics that enact constant temperature  $T = 1/\beta$ .

There are several methods, see, e.g. Ref.<sup>16</sup> to enact constant  $T$ . The one that we will adopt here, a so-called Nosé-Hoover chain thermostat, is widely used because it performs well in a wide variety of systems and it scales to very large systems. Scaling considerations are important because they signal the prospect for high performance implementations of the current approach to the giga-voxel resolution that has been realized with conventional topology optimization<sup>3</sup>.

The Hamiltonian of the system  $\mathcal{H}$  with one constraint (the volume constraint) which is coupled with a Nosé-Hoover chain of length  $N_c$  is

$$\mathcal{H}_{NHC} = \mathcal{H} + \sum_{k=1}^{N_c} \frac{1}{2} Q_k v_{s_k}^2 + (N-1) T_{\text{target}} s_1 + \sum_{k=2}^{N_c} T_{\text{target}} s_k \quad (\text{A4})$$

where  $k^{\text{th}}$  Nosé position,  $s_k$ , is defined as,

$$\dot{s}_k = v_{s_k}; \quad k = 1, \dots, N_x$$

where  $v_{s_k}$  is the  $k^{\text{th}}$  Nosé velocity,  $Q_k$  is the  $k^{\text{th}}$  Nosé mass,  $T_{\text{target}}$  is the temperature we want to hold the system in, and it is understood that  $v_{s_{M+1}} = 0$ <sup>37,39,40</sup>. Working from Eq. (A4), Hamilton's equations give the equations of motion for all particles as first-order differential equations<sup>37,38</sup>.

In general terms, the Nosé-Hoover chain thermostat works by coupling the “particles” that represent the material distribution to an auxiliary set of “particles” that function as a heat bath. The material distribution particles interact with the heat bath particles in a specific manner that allows for an exchange of energy between the two that replicates the effectiveness of constant temperature.

A stable numerical implementation of integrating the equations of motion can be achieved using a symplectic integrator<sup>37,41</sup> and the Lagrange multiplier must be computed at each time-step such that the particle positions (densities) satisfy the volume constraint<sup>37</sup>.



## Appendix B: Sites Dynamics

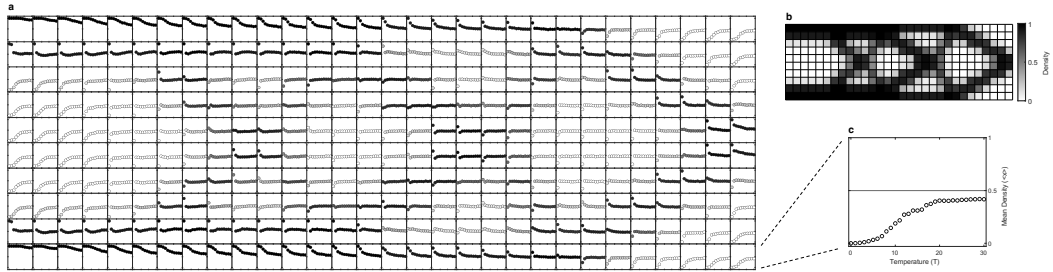


FIG. A1. **Mean density vs  $T$  for all sites for a cantilever beam in 2D.** Fig. 2 (main text) panels f,h,j,l showed mean density vs  $T$  for selected material sites. (a) plots mean density vs  $T$  for all material sites of the cantilever beam design which is shown in (b). Data points in (a) are shaded by the density of the corresponding site in the ultimate design in (b). (c) magnifies the results from a single site to show the density and temperature scales used throughout the individual site plots in (a).

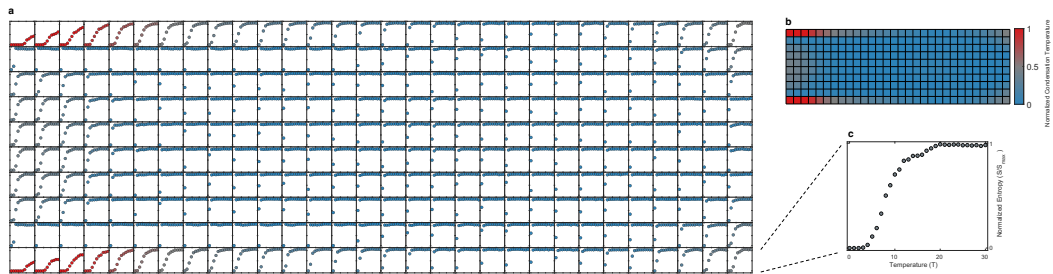


FIG. A2. **Normalized entropy density vs  $T$  for all sites for a cantilever beam in 2D.** Fig. 2 (main text) panels g,i,k,m showed entropy density vs  $T$  for selected material sites. (a) plots entropy density vs  $T$  for all material sites of the cantilever beam design shown in (b). Data points in (a) are shaded by the density of the corresponding site in the ultimate design in (b). (c) magnifies the results from a single site to show the entropy and temperature scales used throughout the individual site plots in (a).

### Appendix C: Entropy Calculation

The entropy of a site's density,  $x_e$ , is calculated using the probability distribution of the site's density within the ensemble of solutions at a given temperature. In the continuous limit, the entropy is expressed as

$$S(x_e) = - \int_0^1 P(x') \log(P(x')) dx';, \quad (\text{A1})$$

where  $P(x)$  represents the probability distribution of the site's density,  $x_e$ , and  $x'$  is the integration variable.

At high temperatures, the entropy reaches its maximum value, corresponding to the absence of a gradient force from the objective function. This condition can be achieved by setting the gradient of the objective function to zero. The maximum entropy values for the cantilever beam problem, as studied in this paper, are shown in Fig. A3.

The differences observed in the maximum entropy values stem from the use of a density filter, a common practice in topology optimization to mitigate numerical instabilities.

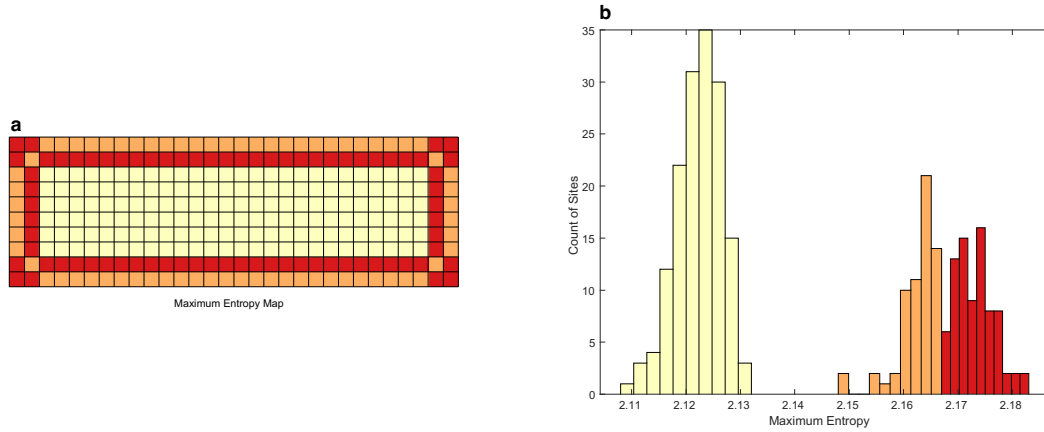


FIG. A3. **Distribution of maximum entropy by site.** Site-specific entropy density is a useful indicator for the condensation process that drives morphogenesis. However, a careful analysis of entropy density at high temperature shows that there is an interaction between the filter and the boundary conditions on the region that lead to a difference in entropy density maxima that varies by  $\lesssim 5\%$  across sites. This variation is plotted in (a), and aggregated as a histogram in (b).

## Appendix D: 3D Cantilever Beam

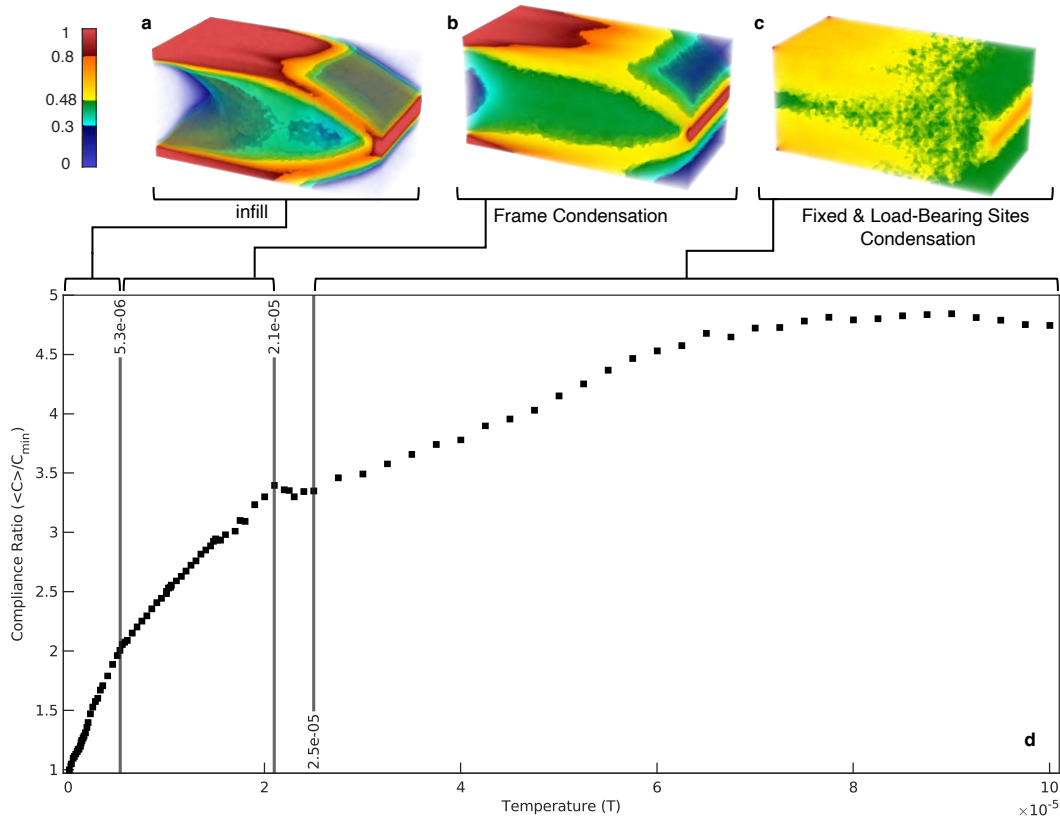


FIG. A4. **Condensation process for morphogenesis of a 3D cantilever beam.** (a-c) show material density using a multicolour material density scale that has been adjusted to maximize illustration of structural details. (A conventional colour scale analogue is shown in the main text.) (d) shows  $\langle C \rangle$  vs  $T$ , which indicates a similar set of condensation regimes as the 2D cantilever beam, albeit at lower  $T$ .

<sup>1</sup>M. P. Bendsøe and N. Kikuchi, "Generating optimal topologies in structural design using a homogenization method," *Computer Methods in Applied Mechanics and Engineering* **71**, 197–224 (1988).

<sup>2</sup>M. Bendsoe and O. Sigmund, *Topology Optimization: Theory, Methods, and Applications* (Springer Berlin Heidelberg, 2013).

<sup>3</sup>N. Aage, E. Andreassen, B. S. Lazarov, and O. Sigmund, "Giga-voxel computational morphogenesis for structural design," *Nature* **550**, 84–86 (2017).

<sup>4</sup>J. Alexandersen, O. Sigmund, and N. Aage, "Large scale three-dimensional topology optimisation of heat sinks cooled by natural convection," *International Journal of Heat and Mass Transfer* **100**, 876–891 (2016).

<sup>5</sup>N. Aage, E. Andreassen, and B. S. Lazarov, "Topology optimization using PETSc: An easy-to-use, fully parallel, open source topology optimization framework," *Structural and Multidisciplinary Optimization* **51**, 565–572 (2015).

<sup>6</sup>B. S. Lazarov, F. Wang, and O. Sigmund, "Length scale and manufacturability in density-based topology optimization," *Archive of Applied Mechanics* **86**, 189–218 (2016).

<sup>7</sup>J. Zhu, H. Zhou, C. Wang, L. Zhou, S. Yuan, and W. Zhang, "A review of topology optimization for additive manufacturing: Status and challenges," *Chinese Journal of Aeronautics* **34**, 91–110 (2021).

<sup>8</sup>S. Cho and H.-S. Jung, "Design sensitivity analysis and topology optimization of displacement-loaded non-linear structures," *Computer Methods in Applied Mechanics and Engineering* **192**, 2539–2553 (2003).

<sup>9</sup>E. Castillo, R. Mínguez, and C. Castillo, "Sensitivity analysis in optimization and reliability problems," *Reliability Engineering & System Safety* **93**, 1788–1800 (2008).

<sup>10</sup>M. Hegwood, R. E. Langendorf, and M. G. Burgess, "Why win-wins are rare in complex environmental management," *Nature Sustainability* **5**, 674–680 (2022).

<sup>11</sup>L. Debnath and D. Bhatta, *Integral Transforms and Their Applications*, 2nd ed. (Chapman & Hall/CRC, Boca Raton, Fla., 2007).

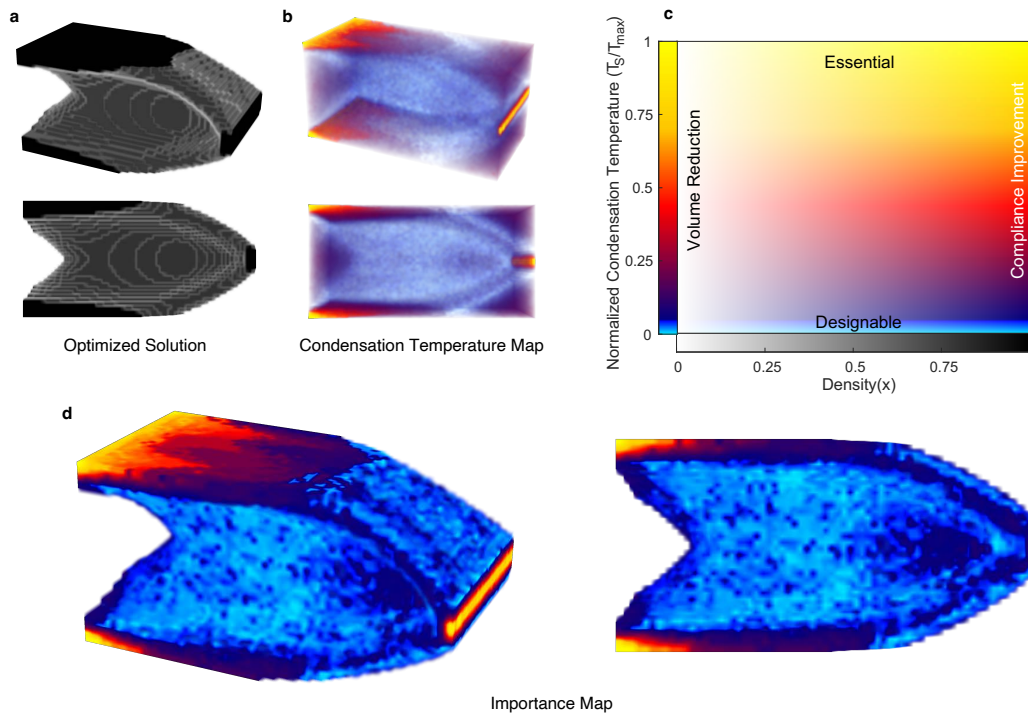


FIG. A5. **Optimized solution, condensation temperature map, and importance map for 3D cantilever beam solution.** (a, b, d) illustrate alternate views in addition to those shown in the main text, which are shaded using a colourmap (c) to facilitate identification of structure.

- <sup>12</sup>L. A. Zadeh, “Theory of Filtering,” *Journal of the Society for Industrial and Applied Mathematics* **1**, 35–51 (1953), 2099062.
- <sup>13</sup>K. Ogata, *Modern Control Engineering*, 5th ed., Prentice-Hall Electrical Engineering Series. Instrumentation and Controls Series (Prentice-Hall, Boston, 2010).
- <sup>14</sup>A. V. Oppenheim, A. S. Willsky, and I. T. Young, *Signals and Systems*, Prentice-Hall Signal Processing Series (Prentice-Hall, Englewood Cliffs, NJ, 1983).
- <sup>15</sup>H. Aliahmadi, R. Perez, and G. van Anders, “Transforming Design Spaces Using Pareto-Laplace Filters,” (2024), 10.48550/ARXIV.2403.00631, arXiv:2403.00631 [cs.CE].
- <sup>16</sup>D. Frenkel and B. Smit, *Understanding Molecular Simulation: From Algorithms to Applications* (Academic Press, San Diego, 1996).
- <sup>17</sup>E. Andreassen, A. Clausen, M. Schevenels, B. S. Lazarov, and O. Sigmund, “Efficient topology optimization in MATLAB using 88 lines of code,” *Structural and Multidisciplinary Optimization* **43**, 1–16 (2011).
- <sup>18</sup>H. Aliahmadi and G. van Anders, “Hyperoptimization for Top88,” (2024), 10.5281/ZENODO.13997110.
- <sup>19</sup>A. Sheedy, H. Aliahmadi, and G. van Anders, “HypOptLib,” (2024), 10.5281/ZENODO.12797384.
- <sup>20</sup>E. Andreassen, B. S. Lazarov, and O. Sigmund, “Design of manufacturable 3D extremal elastic microstructure,” *Mechanics of Materials* **69**, 1–10 (2014).
- <sup>21</sup>J. Gao, H. Li, L. Gao, and M. Xiao, “Topological shape optimization of 3D micro-structured materials using energy-based homogenization method,” *Advances in Engineering Software* **116**, 89–102 (2018).
- <sup>22</sup>J. Xu, L. Gao, M. Xiao, J. Gao, and H. Li, “Isogeometric topology optimization for rational design of ultra-lightweight architected materials,” *International Journal of Mechanical Sciences* **166**, 105103 (2020).
- <sup>23</sup>P. I. Borel, A. Harpøth, L. H. Frandsen, M. Kristensen, P. Shi, J. S. Jensen, and O. Sigmund, “Topology optimization and fabrication of photonic crystal structures,” *Optics Express* **12**, 1996 (2004).
- <sup>24</sup>L. F. Frellsen, Y. Ding, O. Sigmund, and L. H. Frandsen, “Topology optimized mode multiplexing in silicon-on-insulator photonic wire waveguides,” *Optics Express* **24**, 16866 (2016).
- <sup>25</sup>S. Zhou and Q. Li, “A variational level set method for the topology optimization of steady-state Navier–Stokes flow,” *Journal of Computational Physics* **227**, 10178–10195 (2008).
- <sup>26</sup>Y. Deng, Z. Liu, P. Zhang, Y. Liu, and Y. Wu, “Topology optimization of unsteady incompressible Navier–Stokes flows,” *Journal of Computational Physics* **230**, 6688–6708 (2011).
- <sup>27</sup>G. H. Yoon, “A new monolithic design approach for topology optimization for transient fluid–structure interaction system,” *Computer Methods in Applied Mechanics and Engineering* **403**, 115729 (2023).
- <sup>28</sup>J. Alexandersen, N. Aage, C. S. Andreasen, and O. Sigmund, “Topology optimisation for natural convection problems,”

- International Journal for Numerical Methods in Fluids **76**, 699–721 (2014).
- <sup>29</sup>J. Glaser, T. D. Nguyen, J. A. Anderson, P. Lui, F. Spiga, J. A. Millan, D. C. Morse, and S. C. Glotzer, “Strong scaling of general-purpose molecular dynamics simulations on GPUs,” *Computer Physics Communications* **192**, 97–107 (2015).
- <sup>30</sup>R. L. Davidchack, R. Handel, and M. V. Tretyakov, “Langevin thermostat for rigid body dynamics,” *The Journal of Chemical Physics* **130**, 234101 (2009).
- <sup>31</sup>O. Sigmund and K. Maute, “Topology optimization approaches: A comparative review,” *Structural and Multidisciplinary Optimization* **48**, 1031–1055 (2013).
- <sup>32</sup>Note: in the continuum, thinking of  $\Omega(C, V)$  as a count can yield an answer that is formally infinite. In practice,  $Z(\beta)$  as defined in Eq. (4) need only be defined up to an overall multiplicative constant, which one can use to absorb any divergence. However, in such cases, one could define  $\Omega$  as a volume, which would amount to the same thing.
- <sup>33</sup>J. Sethna, *Statistical Mechanics: Entropy, Order Parameters, and Complexity* (Oxford University Press, USA, 2021).
- <sup>34</sup>D. P. Landau and K. Binder, *A Guide to Monte Carlo Simulations in Statistical Physics*, fifth edition ed. (Cambridge University Press, Cambridge, United Kingdom ; New York, NY, 2020).
- <sup>35</sup>Note that it is possible to express Eq. (4) via the continuum form of the design field  $x$ . In that form,  $Z(\beta)$  would be a version of what is referred to as a statistical field theory in physics, see, e.g. Ref.<sup>46</sup>. However, the field representation would require us to introduce a significant amount of notation that we will quickly dispense when we go to the finite element version for ease of implementation.
- <sup>36</sup>L. D. Landau and E. M. Lifshitz, *Statistical Physics, Part 1*, 3rd ed. (Butterworth-Heinemann, Oxford, 1980).
- <sup>37</sup>S. Jang and G. A. Voth, “Simple reversible molecular dynamics algorithms for Nosé–Hoover chain dynamics,” *The Journal of Chemical Physics* **107**, 9514–9526 (1997).
- <sup>38</sup>L. D. Landau and E. M. Lifshitz, *Mechanics*, 3rd ed. (Butterworth-Heinemann, Oxford, 1976).
- <sup>39</sup>M. Tuckerman, B. J. Berne, and G. J. Martyna, “Reversible multiple time scale molecular dynamics,” *The Journal of Chemical Physics* **97**, 1990–2001 (1992).
- <sup>40</sup>G. J. Martyna, M. E. Tuckerman, D. J. Tobias, and M. L. Klein, “Explicit reversible integrators for extended systems dynamics,” *Molecular Physics* **87**, 1117–1157 (1996).
- <sup>41</sup>T. Yamamoto, “Comment on ‘Comment on ‘Simple reversible molecular dynamics algorithms for Nosé–Hoover chain dynamics’ ” [J. Chem. Phys. 110, 3623 (1999)],” *The Journal of Chemical Physics* **124**, 217101 (2006).
- <sup>42</sup>S. Hussain and A. Haji-Akbari, “Studying rare events using forward-flux sampling: Recent breakthroughs and future outlook,” *The Journal of Chemical Physics* **152**, 060901 (2020).
- <sup>43</sup>N. Goldenfeld, *Lectures on Phase Transitions and the Renormalization Group* (Addison-Wesley, Reading MA, 1992).
- <sup>44</sup>J. Anderson, C. Lorenz, and A. Travesset, “General purpose molecular dynamics simulations fully implemented on graphics processing units,” *Journal of Computational Physics* **227**, 5342–5359 (2008).
- <sup>45</sup>E. T. Jaynes, “Information theory and statistical mechanics,” *Physical Review* **106**, 620–630 (1957).
- <sup>46</sup>M. Kardar, *Statistical Physics of Fields* (Cambridge University Press, 2007).
- <sup>47</sup>S. Kirkpatrick, C. D. Gelatt, and M. P. Vecchi, “Optimization by simulated annealing,” *Science (New York, N.Y.)* **220**, 671–680 (1983).
- <sup>48</sup>Ruszczyński, Andrzej, *Nonlinear Optimization* (Princeton University Press, Princeton NJ, 2006).
- <sup>49</sup>W. Li and X. S. Zhang, “Computational morphogenesis for liquid crystal elastomer metamaterial,” *npj Computational Materials* **10**, 125 (2024).
- <sup>50</sup>J. Liu, A. T. Gaynor, S. Chen, Z. Kang, K. Suresh, A. Takezawa, L. Li, J. Kato, J. Tang, C. C. L. Wang, L. Cheng, X. Liang, and Albert C. To, “Current and future trends in topology optimization for additive manufacturing,” *Structural and Multidisciplinary Optimization* **57**, 2457–2483 (2018).
- <sup>51</sup>H. Ohmori, “Computational Morphogenesis: Its Current State and Possibility for the Future,” *International Journal of Space Structures* **26**, 269–276 (2011).
- <sup>52</sup>A. A. Klishin, A. Kirkley, D. J. Singer, and G. van Anders, “Robust design from systems physics,” *Scientific Reports* **10**, 14334 (2021).
- <sup>53</sup>C. Shannon, “A mathematical theory of communication,” *Bell System Technical Journal* **27**, 379–423, 623–656 (1948).
- <sup>54</sup>A. A. Klishin, C. P. Shields, D. J. Singer, and G. van Anders, “Statistical physics of design,” *New Journal of Physics* **20**, 103038 (2018).
- <sup>55</sup>J. Wu, O. Sigmund, and J. P. Groen, “Topology optimization of multi-scale structures: A review,” *Structural and Multidisciplinary Optimization* **63**, 1455–1480 (2021).
- <sup>56</sup>B. Zhu, X. Zhang, H. Zhang, J. Liang, H. Zang, H. Li, and R. Wang, “Design of compliant mechanisms using continuum topology optimization: A review,” *Mechanism and Machine Theory* **143**, 103622 (2020).